Journal of the European Ceramic Society 39 (2019) 705–717

Contents lists available at ScienceDirect

Journal of the European Ceramic Society

journal homepage: www.elsevier.com/locate/jeurceramsoc

Original Article

Material removal mechanism of laser-assisted grinding of RB-SiC ceramics and process optimization

Zhipeng Li[a], Feihu Zhang[a], Xichun Luo[b,*], Wenlong Chang[b], Yukui Cai[b], Wenbin Zhong[b], Fei Ding[b]

[a] School of Mechatronics Engineering, Harbin Institute of Technology, Harbin, China
[b] Centre for Precision Manufacturing, DMEM, University of Strathclyde, Glasgow, UK

ARTICLE INFO

Keywords:
Laser assisted grinding
Temperature prediction
Material removal mechanism
Surface integrity
Optimization

ABSTRACT

Laser-assisted grinding (LAG) is a promising method for cost-effective machining of hard and brittle materials. Knowledge of material removal mechanism and attainable surface integrity are crucial to the development of this new technique. This paper focusing on the application of LAG to Reaction Bonded (RB)-SiC ceramics investigate the material removal mechanism, grinding force ratio and specific grinding energy as well as workpiece surface temperature and surface integrity, together with those of the conventional grinding for comparison. Response surface method and genetic algorithm were used to optimize the machining parameters, achieving minimum surface roughness and subsurface damage, maximum material removal rate. The experiments results revealed that the structural changes and hardness decrease enhanced the probability of plastic removal in LAG, therefore obtained better surface integrity. The error of 3-D finite element simulation model that developed to predict the temperature gradient produced by the laser radiation is found to be within 2.7%–15.8%.

1. Introduction

Owing to low density, excellent corrosion and wear resistance, as well as high temperature strength, advanced structural ceramics have been widely applied in engineering systems for critical components [1–3]. However, their inherent high hardness and low fracture toughness characteristics are also a stumbling block to make damage-free ceramics part. Diamond grinding, as a major process for machining ceramics, suffers from low material removal rates and high tool wear [4]. Therefore, some new machining processes such ultrasonic grinding [5] and laser-assisted grinding (LAG) [6] have been developed in order to increase material removal rates, prolong the tool service life and enhance the surface integrity of the workpiece. In LAG, the workpiece was locally heated by laser prior to material removal by grinding wheel. The heat will help to reduce the yield strength of workpiece below its fracture strength and promote plastic deformation instead of brittle fracture. Chang and Kuo [7] conducted a study on LAM Al_2O_3 ceramics in which the cutting force, surface temperature, surface integrity and wear were measured. Their research reveals that the feed and thrust cutting forces can be reduced by 22% and 20%, respectively, and gain better surface quality than conventional diamond grinding. Again, Guerrini et al. [8] showed that the reduction of peak and average machining forces were approximately 26%–27% when the grinding tests were performed on sintered reaction bonded silicon nitride workpiece which possessing thermal crack induced by previous laser treatment. In LAM Magnesia-partially-stabilized zirconia, Pfefferkorn et al. [9] testified that the tool life can be effectively prolonged with increased material removal temperature. Likewise, Wang et al. [10] found that the machined surface quality is improved in LAM of Al_2O_3p/Al compared with conventional cutting and the tool wear can be reduced by 20–30%.

In terms of material removal mechanism, Lee and co-workers [11] investigated the microstructure variations in LAM of silicon nitride and found that the surface of the specimen was oxidized at a high temperature and formed an amorphous silicate. This was the reason for hardness reduction. While in the study of LAM of silicon nitride, Lei and co-workers characterized the plastic deformation of silicon nitride in the shear deformation zone and found viscous flow of the glassy grain-boundary phase material and reorientation of the β-Si_3N_4 grains. In addition, the stress decreases with the increase of workpiece temperature [12,13]. This result was also supported by aforementioned reference [7]. These researchers also found that the intergranular glassy phase flow and redistribute when temperature excessed glassy transition point i.e. 850 °C during LAM of Al_2O_3 ceramic.

* Corresponding author.
E-mail address: xichun.luo@strath.ac.uk (X. Luo).

https://doi.org/10.1016/j.jeurceramsoc.2018.11.002
Received 9 September 2018; Received in revised form 1 November 2018; Accepted 2 November 2018
Available online 03 November 2018

Moreover, in the field of theoretical analysis, Dandekar et al. [14] who applied a multi-scale model to predict the subsurface damage in a particle reinforced metal matrix composite after LAM. They proposed that the combination of molecular dynamics parameterized traction-separation laws and finite element can get favourable agreement between predicted subsurface damage and experimental results. Ramesh Singh et al. [15] investigated the heat-affected zone microstructure and microhardness changes generated by different laser scanning speeds. And a 3-D transient finite element model for a moving Gaussian laser heat source is developed to predict the temperature distribution in the workpiece.

So far study of LAG of RB-SiC ceramics is very rare, especially the material removal mechanism. To fill this gap, this paper will build a 3-dimensional finite element simulation model for laser heating in the LAG process to characterize and predict the thermal gradient, thermal history and the heat affected zone produced by the laser radiation. This simulation will be used to predict the temperature distribution under different laser power. This will help to select appropriate laser power which can result in the high surface temperature to soften work material without melting the workpiece or leaving undesirable microstructural alteration. The effect of temperature on the hardness of RB-SiC ceramics will be analysed. Both LAG and CG experiments were conducted under the same machining conditions. The differences between LAG and CG in terms of material removal mechanism, surface/subsurface damage and grinding force will be analysed. To implement this machining process the paper will also develop empirical process model response surface method (RSM) and genetic algorithm (GA) optimisation approach to determine process parameters to obtain high quality (low surface roughness R_a and depth of subsurface damage D_{sub}) machined surface while achieving high machining efficiency. Confirmation machining trials will be conducted to validate the obtained optimum results and prove the effectiveness of RSM process model and GA optimization model.

2. Thermal modelling

2.1. Modelling and settings

To predictive the temperature distribution in the RB-SiC ceramics that induced by laser radiation, a three-dimensional transient heat conduction model was build based on a Gaussian heat source applied to the workpiece surface. The Gaussian-distributed heat flux is given by:

$$q_{(x,y)} = \frac{2P_{laser}}{\pi R_b^2}\exp(-\frac{2r^2}{R_b^2}) \quad (1)$$

Where q is the heat flux at the position (x, y), r is the radial distance from the laser radiation center, R_b is the radius of laser beam, P_{laser} is the product of incident laser power and average absorptivity of the RB-SiC ceramics which is equal to 0.73 [16]. The heat generation was calculated by adopting the finite element method. Besides, in order to simplify the simulation model, the RB-SiC ceramic material is assumed to be homogeneous and isotropic. Meanwhile, the thermal properties of RB-SiC ceramics are considered as functions of the temperature [17]. Hence, three-dimensional heat diffusion equation in Descartes coordinates is expressed as:

$$\frac{\partial^2 T}{\partial x^2} + \frac{\partial^2 T}{\partial y^2} + \frac{\partial^2 T}{\partial z^2} = \rho c_p \frac{\partial T}{k\partial t} \quad (2)$$

Where T, ρ, c_p are the temperature filed, density and thermal capacity, respectively. Assuming the initial temperature for the workpiece is equal to the room temperature, therefore, the initial condition at time $t = 0$ is given as:

$$T(x, y, z, 0) = T_0 \quad (3)$$

The boundary condition for the problem that described in Eq. (2) can be expressed by:

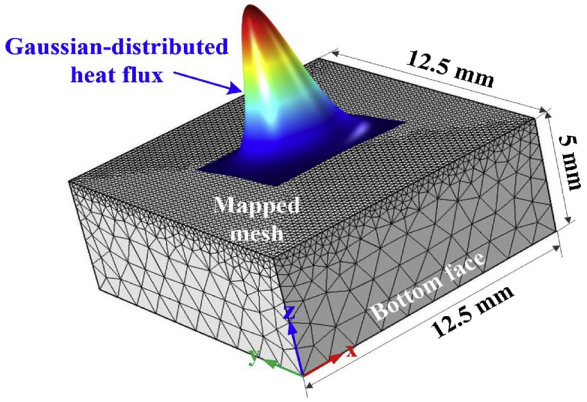

Fig. 1. Finite element model of laser heating RB-SiC ceramic workpiece.

$$k\frac{\partial T}{\partial n} - q + h(T - T_0) + \sigma\varepsilon(T^4 - T_0^4) = 0 \quad (4)$$

Where h is convective heat transfer coefficient that equal to 10 W/m^2/K, σ is Stefan-Boltzmann constant which equal to 5.67 × 10^{-8} W/m^2 K^4 and ε is emissivity that equal to 0.73 [16,18].

The model is implemented by using the COMSOL Multiphysics 5.0 software. Fig. 1 presents the geometric model including the workpiece and Gaussian-distributed heat source. Note that the upper layer surface where the laser incident place was mapped with much finer than the bottom surface, which setting could help to capture the temperature gradients as accurately as possible. The minimum size of finite elements is 0.168 mm while the maximum finite elements is 0.595 mm. The size of the mapped element is 12.5 mm along the X-axis (width) and the Y-axis (length), and 5 mm along the Z-axis (Height). The simulated Gaussian-distributed heat source diameter is 3 mm which parameter is equal to the following experimental laser beam settings. Table 1 presents the main physical and mechanical properties of the RB-SiC material (supplied by Goodfellow Cambridge Ltd).

3. Experimental work

3.1. Machining conditions

The test specimen of RB-SiC material used in this study was offered by Goodfellow Cambridge Ltd. (UK). The RB-SiC workpiece has a dimension of 12.5 × 12.5 × 5 mm. In order to avoid the influence of surface defects of work material, the RB-SiC specimen was polished with cerium dioxide powders (grit size of 1 μm) until its surface roughness Ra is less than 5 nm. The final polished surface topography was shown in Fig. 2. From the energy spectrum results, it can conclude that the dark particles are SiC phase (90%) which are embedded in a remaining Si phase (10%). In addition, the structure of main was analysed in Section 4.2 using XRD.

Table 1
Workpiece material properties.

Items	RB-SiC
Elastic modulus (GPa)	390
Vickers hardness (kgf·mm^{-2})	3000
Compressive strength (MPa)	2000
Fracture toughness K_{IC} (MPa·m$^{1/2}$)	4.0
Thermal Expansion Coeff. × 10^{-6}/°C	3
Thermal conductivity (W/mK)	150
Melting point (K)	3000
Specific heat Capacity (J/kgK)	1100
Density ρ (g/cm^3)	3.1

Note: the parameters listed in Table 1 are supplied by Goodfellow Cambridge Ltd.

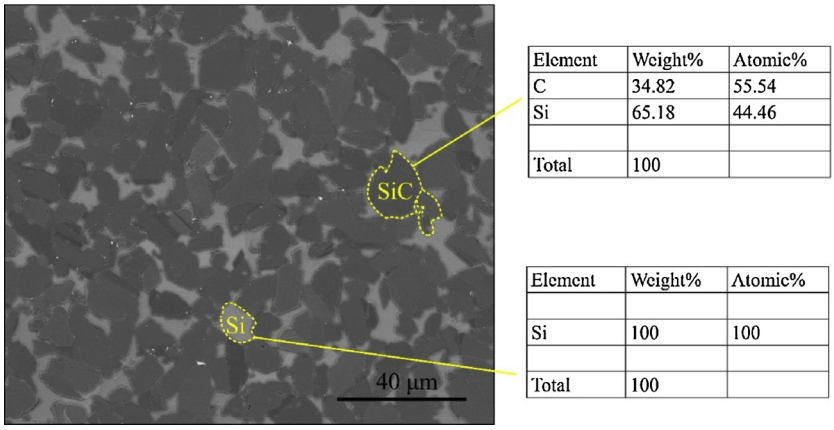

Element	Weight%	Atomic%
C	34.82	55.54
Si	65.18	44.46
Total	100	

Element	Weight%	Atomic%
Si	100	100
Total	100	

Fig. 2. SEM image of surface morphology of the polished specimen and energy spectrum analysis of the corresponding area.

In this paper, we focus on the effect of temperature on the hardness of RB-SiC ceramics. Therefore, four groups of laser radiation tests were conducted on RB-SiC ceramics under the laser powers of 20 W, 30 W, 50 W and 70 W with a dwell time of 60 s. The indentation tests were performed 5 s after laser heating on each laser radiated material surface by Vickers micro-hardness tester (MicroWizhard), at a load of 300 kgf, with a loading time of 5 s, holding time of 10 s and unloading time 5 s.

After that, the LAG and CG experiments are performed on a hybrid ultra-precision micromachine (Micro-3D) without using coolant. Fig. 3 shows a schematic diagram of LAG and its experimental setup. The RB-SiC workpieces are clamped on the worktable through a vice protected by heat shield. Metallic bond diamond abrasive grinding wheels (6 mm wheel diameter with grit size of 64 μm and 100% concentration) are adopted in the machining trials. A fibre laser with wavelength of 1064 nm (YLR-200-MM-AC-11) is used in the LAG process. The focusing lens is mounted on the work spindle and connected to the laser via optical fibre, allowing arbitrary motion between the laser spot and workpiece. The intense laser radiation is projected peripheral to the machining area onto the surface of sample in front of the engaging grinding wheel. The laser spot diameter is about 3 mm.

Before grinding, each workpiece surface with the dimension of 12.5 × 12.5 mm is scanned with laser for 60 s with a feed rate of 12.5 mm/min. Besides, in the whole grinding experiments, 5 s was left before the grinding wheel contact with the workpiece by controlling the space distance. During grinding process, the grinding forces are measured by a 3-component piezoelectric dynamometer Kistler 9129 AA. An infrared thermometer (IR-750-EUR BEHA-AMPROBE) is used to concurrently measure the temperature of the workpiece surface, whose range is −50 to 1550 °C with a ± 1.8% accuracy and a 0.25 s response time. The machined surface topography is characterized by a scanning electron microscope (SEM) (Dual beam FEI Helios Nanolab 600i). The structural analysis on the surface of RB-SiC ceramic before and after laser assisted grinding was performed by using Bragg-Brentano X-ray diffraction (XRD) with *CuKα* radiation (Rigaku SmartLab). The machined surface roughness R_a is measured by a white light interferometer (Zygo cp-200) at five different locations and then took the average as the final results (as shown in Table 4). Cross section polishing will be conducted by using IB-09020CP ion polisher in order to examine depth of subsurface damages and distribution of micro-cracks underneath the ground surface. To reduce random error, four different positions are measured for each specimen.

3.2. Experimental design

3.2.1. Comparison trials between LAG and CG

These experiments are designed to gain clear understanding of the material removal mechanism of RB-SiC ceramics in LAG through comparison with CG in terms of machined surface roughness R_a, surface/subsurface damage, grinding force ratios and specific grinding energy. The operating conditions listed in Table 2 are used in the comparison experiments which including laser power (*P*), feed rate (*F*), wheel speed (*V*), depth of cut (*D*). It is important to note that in the experiments the feed rate of the worktable is equal to the laser beam scanning velocity. Each set of grinding conditions will be repeated four times and the averaged value will be taken as the final result.

3.2.2. Optimization tests

In order to optimize the processing parameters, response surface

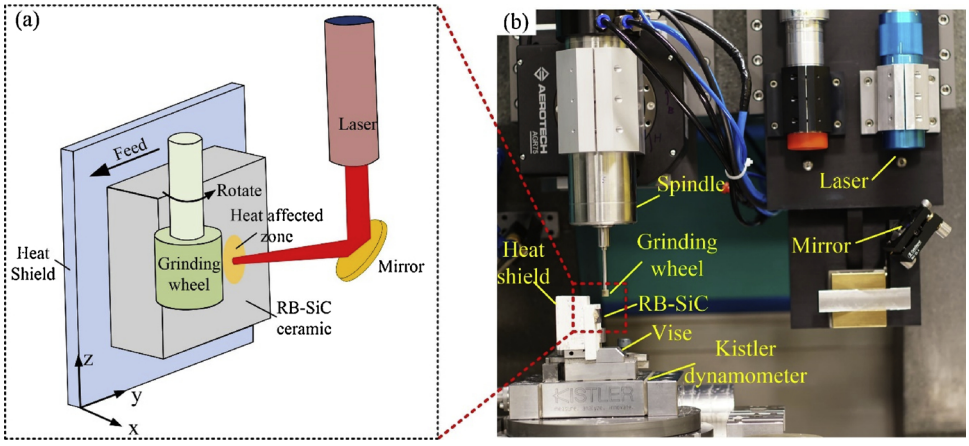

Fig. 3. Illustration of laser-assisted grinding (a) Schematic diagram and (b) Experiment setup.

Table 2
Operating parameters for LAG and CG comparison experiments.

Test	Operation Conditions			
	Laser power P (W)	Wheel speed V (rpm)	Feed rate F (mm/min)	Depth of cut D (μm)
Case 1	20	6000	20	15
Case 2	30	8000	15	10
Case 3	50	10,000	10	8
Case 4	70	14,000	5	5

Table 3
Levels of independent factors.

Factors	Levels of factors				
	−2	−1	0	1	2
P	10	20	30	40	50
V	6000	8000	10,000	12,000	14,000
F	5	15	25	35	45
D	2.5	5	7.5	10	12.5

Table 4
L31 design matrix for experiments and measured results of surface roughness R_a and depth of subsurface damage.

	Levels of factors Output responses					
	P	V	F	D	R_a (μm)	D_{sub} (μm)
1	−1	−1	−1	−1	1.589	8.3
2	0	0	2	0	1.297	6.5
3	−1	−1	1	−1	1.208	5.9
4	1	−1	−1	−1	1.015	6.2
5	0	0	0	0	0.988	5.7
6	1	−1	1	1	1.305	7.6
7	−1	1	1	−1	1.401	7.7
8	0	−2	0	0	0.867	5.2
9	1	−1	−1	1	1.503	8.3
10	1	−1	1	−1	0.556	3.6
11	0	0	0	0	1.178	6.8
12	0	0	0	0	1.195	6.2
13	1	1	1	−1	0.997	6.3
14	0	0	0	0	1.253	7.2
15	0	0	0	−2	0.895	5.8
16	−1	−1	1	1	1.357	8.6
17	0	0	0	0	1.108	6.1
18	0	2	0	0	1.325	8.3
19	1	1	1	1	1.465	8.4
20	−1	1	−1	−1	1.634	9.1
21	0	0	0	0	1.023	6.3
22	2	0	0	0	1.340	5.9
23	−1	−1	−1	1	1.784	10.2
24	1	1	−1	−1	1.104	6.8
25	0	0	0	0	1.065	5.8
26	0	0	0	2	2.240	9.2
27	−1	1	−1	1	1.976	9.5
28	−2	0	0	0	1.845	11.8
29	1	1	−1	1	1.593	8.1
30	−1	1	1	1	1.685	10.9
31	0	0	−2	0	1.285	9.4

methodology (RSM) [19,20] is firstly adopted to model the LAG process. Based on Central Composite Designs method, the experiments that consist of 31 runs for computation are designed with five levels of factors for four machining parameters. Table 3 presents various process parameters and their corresponding levels. The output responses data are outlined in Table 4. In the current work, the relationship between the controllable machining parameters can be given by:

$$Y = \phi(P, V, F, D) \pm \varepsilon \quad (5)$$

Where Y is the response function, ε is the system error. In this study the machined surface roughness R_a and depth of subsurface damage are chosen as the response functions.

Based on RSM the second-order response surface can be expressed as:

$$Y = \beta_0 + \sum_{i=1}^{k} \beta_i X_i + \sum_{i,j}^{k} \beta_{ij} X_i X_j + \sum_{i}^{k} \beta_{ii} X_i^2 + \varepsilon, (i < j) \quad (6)$$

Where β_0, β_i, β_{ii}, β_{ij} are the regression coefficients, and its values are calculated by least square method. X_i represents independent factors parameters.

3.2.3. Genetic algorithm optimization (GA)

To make the LAG process cost-effective the optimised machining parameters need guarantee not only high machined surface quality but also high machining efficiency. In this context, Genetic Algorithm (GA) optimization approach is adopted in this research. The method started with a population of random regimes to optimise processing parameters of P, F, V and D. The objective functions are the response functions shown in Eq. (5). The problem of optimisation then becomes how to maximize the value of material removal rate within a set of constraints on surface roughness R_a, subsurface damages and input variables. In this research GA is implemented using the optimization Toolbox (MATLAB 2012a) with double vector of population type, 100 generations, population size of 100 with scattered crossover function of 0.8, mutation probability of 0.001, rank scaling function and stochastic uniform option.

4. Results and discussions

4.1. Model validation

Fig. 4 shows the simulated temperature distribution as the change of time in the RB-SiC ceramic induced by a 70 W laser power radiation. It can be seen that the heat distributed in a semicircular region, and the temperature increased with time. When the time approached 60 s, the maximum temperature at the centre of Gaussian heat source is about 2045 K, and the temperature decays to 1407 K at the bottom of the workpiece. To validate the simulation results, the measured results of transient temperature and the predicted temperature as a function of the distance from the laser beam centre were plotted in Fig. 5. Five temperature readings were taken at each location. The error bars in the figures represent one standard deviation of the measurements. The error between prediction value and measured are mostly falling within 2.7%–15.8%. It is evident that the temperature predicted by the finite element method has a good consistent with the measured value. Besides, it can be observed that the on temperature gradient is sensitive to the laser power. The mean value of temperature increased from 752 K to 1758 K when the laser power increased from 20 W to 70 W.

On the other hand, in order to testify the effect of heat on material properties, the changes of micro-hardness of the laser radiation surface were measured using Vickers hardness tester. As shown in Fig. 6, the received specimen has a hardness value of 2920 Hv before the pre-heat, and its hardness significantly decreased with the pre-heating. In addition, the hardness tended to decrease from 2917 Hv to 2483 Hv with the increase of laser power from 20 W to 70 W. What's more, the surface topography after 60 s laser radiation at laser powers of 50 W and 70 W were shown in Fig. 7. No micro crack was found when the laser power was set as 50 W (Fig. 7a). There were much more pores can be occasionally seen in the radiation surface, which came from both material defects and laser radiation. On the contrary, if the laser power increased to 70 W, a few micro-cracks induced by thermal stress could be observed in Fig. 7b. The contribution of such a small number of micro-cracks to hardness change is limited. Therefore, it is reasonable to believe that the RB-SiC ceramic has been thermal softened by the laser radiation and its degree increased with the increase of temperature.

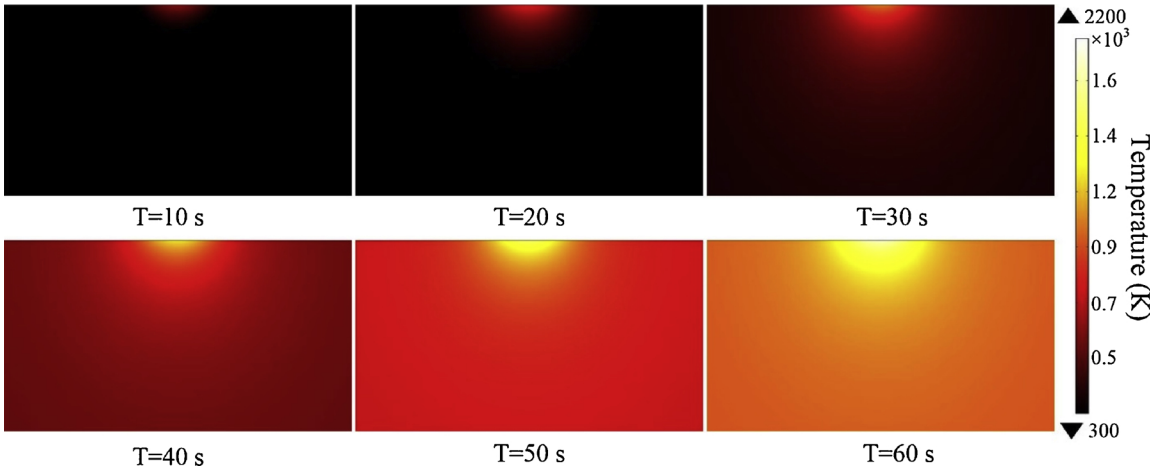

Fig. 4. The variation of simulated temperature distribution with different time in the RB-SiC ceramic under 70 W laser radiation.

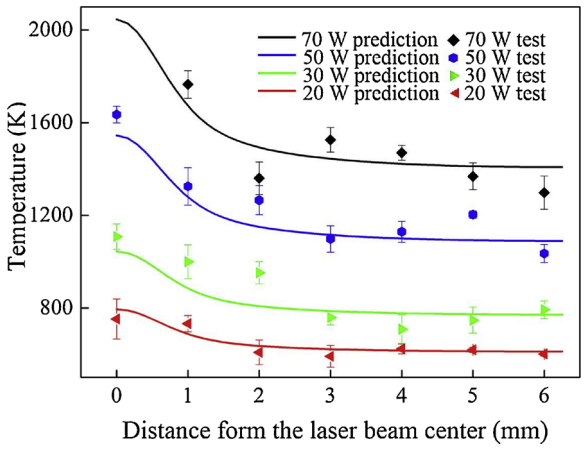

Fig. 5. Variation of surface temperature by laser radiation.

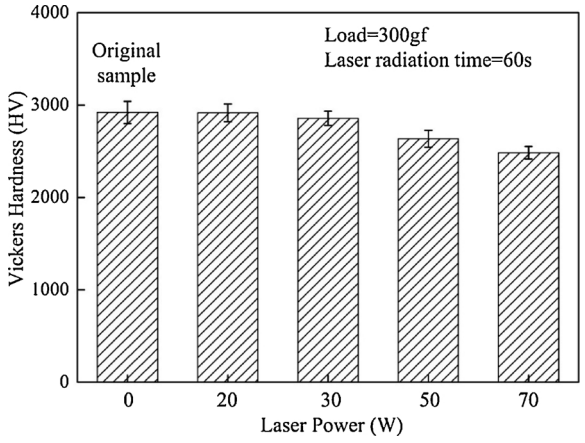

Fig. 6. The Vickers hardness changes with the different laser power radiation.

4.2. Comparison between LAG and CG

4.2.1. Material removal mechanism

Fig. 8 shows the typical SEM images of the residual topography of RB-SiC ceramics after machined by CG and LAG, which obtained under the same machining parameters of Case 3 as listed in Table 2. Obvious irregular pits and sharp edges induced by fracture can be observed on the machined surface by CG (shown in Fig. 8a–c). In contrast, LAG machined surface (Fig. 8d and e) presents smoother regions with ductile streaks and less sharp pits, which are different with CG machined surface. In the LAG process, the temperature at the centre of the laser radiated zone is about 1544 K as shown in Fig. 5. The smeared area that covered with fine molten debris is observed in the enlarged view (as shown in Fig. 8f). This means that plastic flow of material are the dominant removal mechanisms in LAG.

Aforementioned differences in LAG and CG can be elaborated by strength degradation that caused by thermal effect in laser radiation. It is well known that when the temperature rising to 800–1700°C in an oxygen-containing atmosphere, the surface layer of ceramics would more likely starts to oxidize [11,21]. As shown in Fig. 8, the EDS measurement results which collected from the LAG surface present that the content ratio of Si and O is near to the ratio of these elements in SiO_2. While on the CG surface, the element of O was not detected. What's more, in order to further assess the structural quality changes before and after LAG, the XRD test was conducted. In XRD pattern (Fig. 9), a broad band at $2\theta = 22.8^{\circ}$ was detected, which confirmed that the amorphous SiO_2 was indeed generated in the LAG process. Note that the SiO_2 is more thermodynamically stable than other style. The chemical reaction process is described by:

$$Si + O_2 \rightarrow SiO_2(g)$$
$$SiC(s) + 2O_2(g) \rightarrow SiO_2(s) + CO_2(g) \quad (7)$$

This result implies that the actual contact area between the grinding wheel grits and workpiece during the grinding process contain SiO_2 compositions in LAG, which possessing lower strength than SiC grain. On the other hand, it has been testified that the hardness of RB-SiC ceramics is reduced with the increase of temperature, which will promote the material prefer to be removed in ductile mode than brittle fracture.

To realize the surface integrity of LAG of RB-SiC ceramics, it is also important to know what happened below the ground surface. Fig. 10 shows the subsurface damages of received sample of RB-SiC ceramic and induced by CG and LAG. In original sample of RB-SiC, there almost no cracks can be observed in the subsurface substrate. In LAG, subsurface damages take the form of tiny lateral-type cracks initiating near surface layer and mostly propagate to the free surface as illustrated in Fig. 10d–f. Nevertheless, CG generate both median cracks and lateral cracks which consist of intensely trans-granular and inter-granular fracture. In addition, such median cracks penetration depth is much deeper than LAG induced subsurface damages as shown in Fig. 10g–i. Such subsurface crack configurations explain why CG caused relatively roughness surface. The extending or interaction of deeper lateral cracks will result in large brittle chips removal and leave fracture pits as seen in Fig. 9a–c. To make the comparison more intuitive, the values of surface roughness R_a and subsurface damages produced in CG and LAG

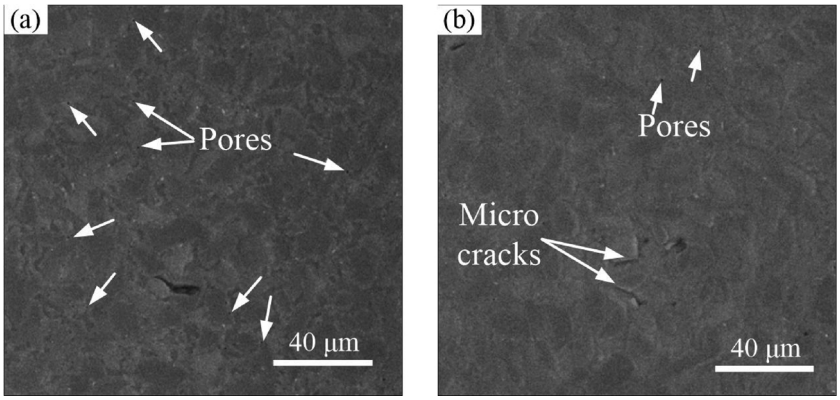

Fig. 7. The surface topography after 60 s of laser radiation at the powers of (a) 50 W (b) 70 W.

was plotted in Fig. 11. It can be found the depth of subsurface damages or the surface roughness that produced in LAG is much lower than that obtained by CG. Meanwhile, it is evidence that the difference of R_a and D_{sub} that produced by LAG and CG increased when the temperature increased from 752 K to 1246 K. However, when the mean value of temperature reached to 1758 K, the difference between LAG and CG was scaled down. In another word, both of R_a and D_{sub} that obtained under the laser power of 70 W are larger that obtained under the laser power of 50 W. This illustrates that increasing laser power does not always result in better surface quality. In this case, high temperature caused by 70 W laser radiation could burn the grinding tools, leading the increase of R_a and D_{sub}. Hence, in order to obtain less surface and subsurface damage, it is necessary to optimize the laser power parameters.

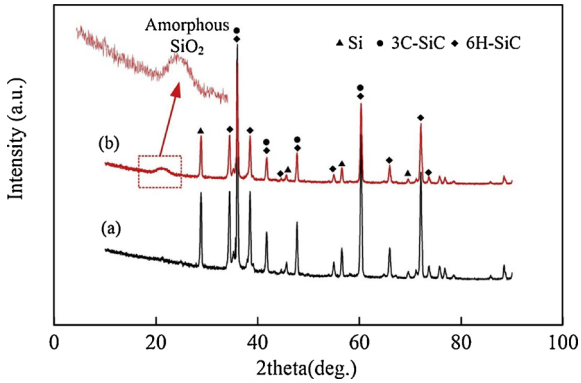

Fig. 9. XRD patterns for RB-SiC ceramic surface: (a) before grinding (b) after LAG.

4.2.2. Grinding force ratios and specific grinding energy

The grinding forces ratios F_n/F_t obtained from the averaged values of four repeated tests are plotted in Fig. 12a. It is apparent that the increasing magnitude of the tangential force is significantly greater than that of the normal force, when the specific removal rates decreased from 5×10^{-3} (case 1) to 0.41×10^{-3} (case 4) mm^3 per mm. This can be explained using chip geometry in conventional grinding [25]. According to Eq. (8), the increasing specific removal rates will increase the maximum undeformed chip thickness (U_{max}), therefore leading more fracture removal behaviour involved.

$$U_{max} = \left[\frac{3}{C \tan\theta}\left(\frac{F}{V}\right)\left(\frac{D}{d_s}\right)^{1/2}\right]^{1/2} \quad (8)$$

Where C is the active cutting edges density, θ is the semi-included angle for the uncut chip cross section, and d_s is the wheel diameter. Furthermore, the grinding force ratios in LAG are smaller than CG excluding the last case. It indicates that the soften effect induced by laser irradiation can decrease the normal indentation force and increase the scratching, ploughing and chips formation influence. However, the abnormal grinding force ratios in Case 4 (maximum temperature

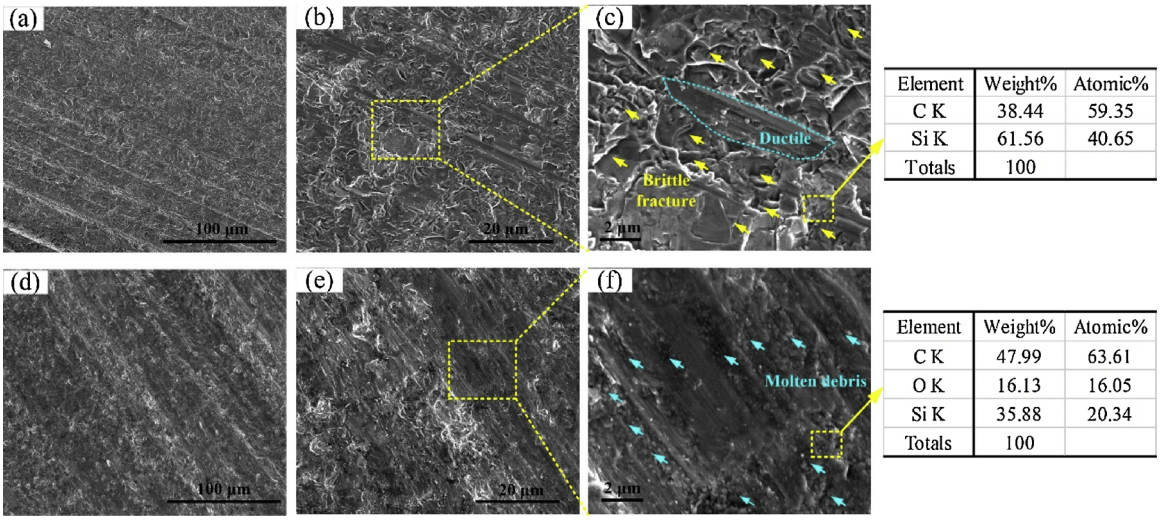

Element	Weight%	Atomic%
C K	38.44	59.35
Si K	61.56	40.65
Totals	100	

Element	Weight%	Atomic%
C K	47.99	63.61
O K	16.13	16.05
Si K	35.88	20.34
Totals	100	

Fig. 8. Typical grinding surface topography under the 10,000 rpm grinding wheel speed, 10 mm/min feed rate and 8 μm depth of cut (a–c) Without laser, (d–f) With 50 W laser power.

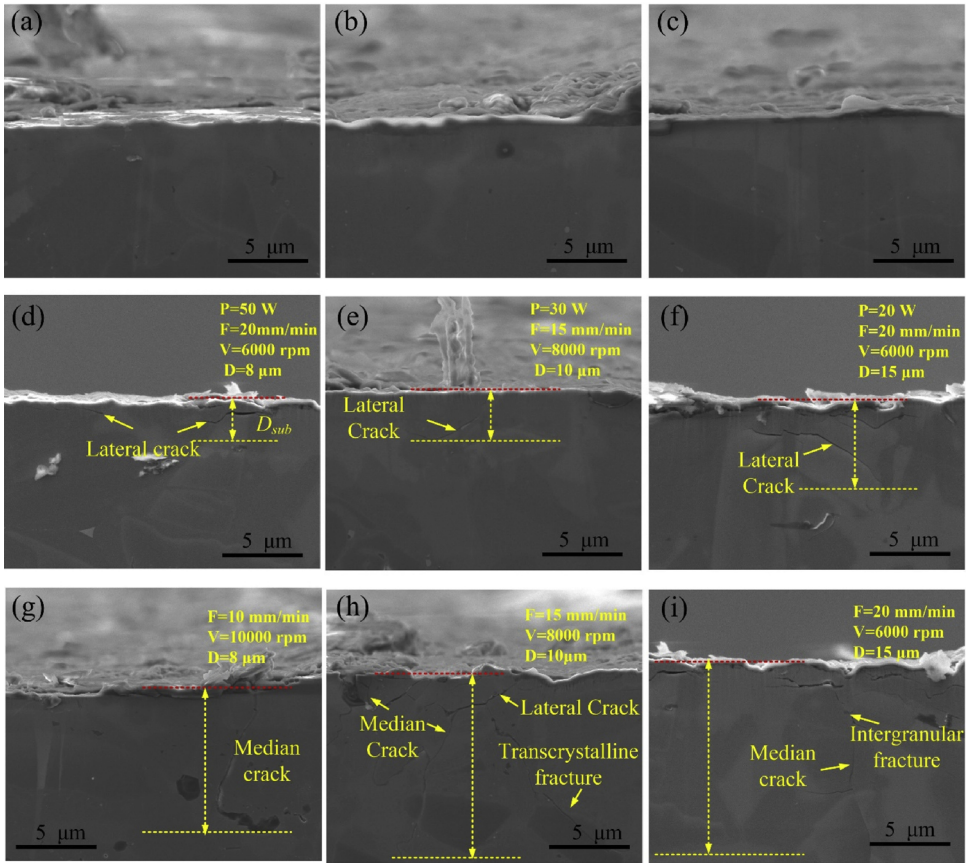

Fig. 10. Typical SEM micrographs showing the subsurface damage observed under different grinding variables (a–c) The received sample of RB-SiC ceramic, (d and e) CG and (g–i) LAG.

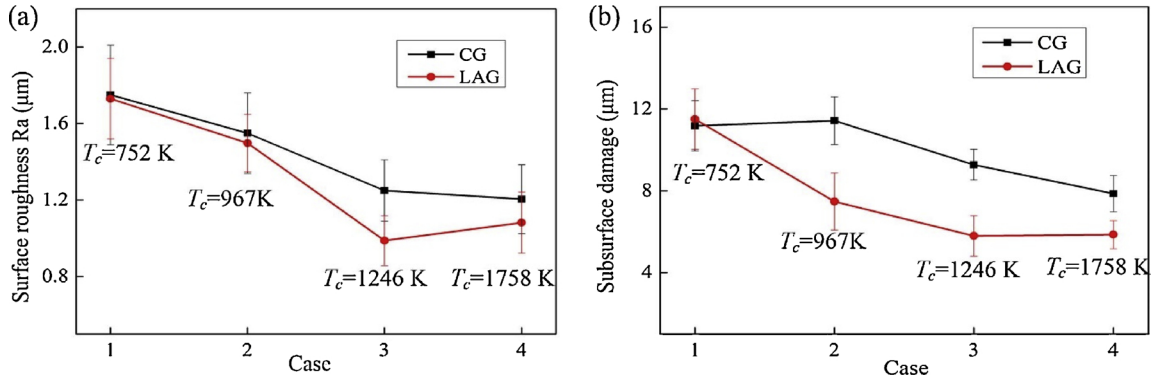

Fig. 11. The measured results of (a) Surface roughness R_a and (b) Subsurface damages induced by LAG and CG.

reached 2045 K) is also due to the burn of grinding wheel and the wear of abrasives, which makes pressing into RB-SiC ceramics hard. This phenomenon is also responsible for the aforementioned results of surface roughness R_a and subsurface damages as shown in Fig. 11.

In addition, the calculated results of specific grinding energy (dividing the measured grinding power by the volumetric removal rate) are shown in Fig. 12b. There is a clear trend associated with the decreasing specific removal rates in both LAG and CG i.e. the specific grinding energy increased with the decrease of specific removal rates. This behavior in specific grinding energy is always expected because the formation of ductile chips needs more energy (chip thickness decreased with the decrease of specific removal rate). Besides, it should be noted that the increments in specific grinding energy for RB-SiC ceramics in LAG is much higher than CG, especially when the laser power increased from 50 W to 70 W. As shown in surface topography measurement results (Fig. 8) that under the same conditions the predominant material removal mode transferred from fracture in LAG to ductile in CG, therefore, the specific grinding energy was consumed more than no involving laser assisted cases. The difference between LAG and CG in grinding force ratios and specific grinding energy illustrated that the laser power is a critical parameter in affecting the processing quality of RB-SiC ceramics.

4.3. ANOVA and effect of grinding variables on response

4.3.1. Modelling of surface roughness R_a and D_{sub}

The measured results of R_a and D_{sub} that obtained from 31 groups of LAG trials were listed in Table 4. To analyse the correlation between the input parameters and their responses, the most suitable quadratic polynomial model was selected to fit the data among various types of

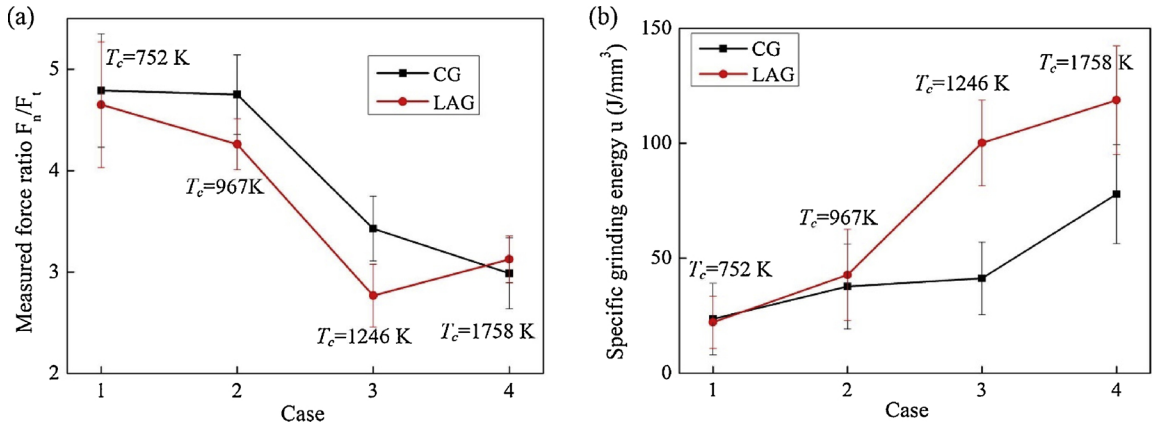

Fig. 12. The measured results of (a) Grinding force ratios F_n/F_t and (b) Specific grinding energy.

regression such as linear, two factorials, quadratic and cubic. After that, ANOVA was applied to check the adequacy of the model by incorporating verification of regression model, model coefficient and lack of fit value [23,24].

ANOVA analysis results presented in Tables 5 (R_a) and 6 (D_{sub}) indicate that the established prediction capabilities of the equations are within reliable interval since R^2 value is 91.27% and 94.63% is for R_a and D_{sub}, respectively. The R^2 coefficient presents the proportion of the total variation in the response predicted by the model, which is defined as the ratio of the regression sum of squares (SSR) and total sum of squares (SST). A high R^2 value greater than 90% ensures a good correlation between the predicted and the experimental results. Moreover, the F-value of model R_a and D_{sub} are 11.94 and 20.14, respectively which implies the model is significant. There is only a 0.01% chance that a "Model F-Value" could occur due to noise. For R_a and D_{sub}, the lack of fit term is not significant compared to the pure error. Consequently, it can be concluded that the R_a and D_{sub} models predicted values has a good agreement with the actual values and a high credibility.

On the other hand, the diagnostic plot Fig. 13 shows that experimental values of R_a and D_{sub} are distributed within the scope of the predicted linear curves. The errors are normally distributed as illustrated in Fig. 14, in which all residual points are falling in straight line. This proves the validity of the developed prediction equations.

Thus, the final equation of surface roughness R_a model was developed as:

$$R_a = 5.7601 - 0.12181P - 0.036896D - 3.8217 \times 10^{-4}V - 0.059236F + 5.5 \times 10^{-5}PD + 1.375 \times 10^{-6}PV + 7.65 \times 10^{-4}PF + 8.825 \times 10^{-6}DV + 5 \times 10^{-6}DF + 4.25 \times 10^{-7}VF + 1.1903 \times 10^{-3}P^2 - 8.15238 \times 10^{-4}D^2 + 1.0913 \times 10^{-8}V^2 + 1.1278 \times 10^{-3}F^2 \quad (9)$$

The final equation of subsurface damage response model was developed as:

$$D_{sub} = 38.42630 - 0.53219P - 0.69792D - 3.61198 \times 10^{-3}V - 0.20656F - 7.5 \times 10^{-4}PD + 1.5625 \times 10^{-6}PV + 8.125 \times 10^{-4}PF + 8.875 \times 10^{-5}DV - 9.25 \times 10^{-3}DF + 1.96875 \times 10^{-5}VF + 6.51042 \times 10^{-3}P^2 + 0.020167D^2 + 1.0651 \times 10^{-7}V^2 + 3.13542 \times 10^{-3}F^2 \quad (10)$$

4.3.2. Effect of the influential factors on the R_a and D_{sub}

Table 5 shows that the individual effect of feed rate is the most significant term for surface roughness R_a as it has the highest F-Value (Lowest P value). Along with the feed rate, the individual effect of laser power, depth of cut and wheel speed, second order effect of laser power (P^2) and feed rate (S^2) are the significant terms as p values are less than 0.05. More directly, the perturbation plots shown in Fig. 15 can depict the changing tendency of responses versus various variables. The

Table 5
ANOVA analysis of surface Roughness R_a.

Source	SS	DF	MS	F-value	P-value	
Model	3.45	14	0.25	11.94	< 0.0001	Significant
P	0.70	1	0.70	34.00	< 0.0001	
D	0.25	1	0.25	12.14	0.0020	
V	0.20	1	0.20	9.76	0.0043	
F	1.43	1	1.43	69.10	< 0.0001	
*P*F*	0.094	1	0.094	4.53	0.0304	
P^2	0.41	1	0.41	19.61	0.0004	
F^2	0.36	1	0.36	17.60	0.0006	
*P*D*	0.00003	1	0.00003	0.0015	0.9142	
*P*V*	0.0012	1	0.0012	0.59	0.4982	
*D*V*	0.031	1	0.031	1.51	0.3427	
*D*F*	2.5E-7	1	2.5E-7	1.21E-5	0.9414	
*V*F*	0.00012	1	0.00012	0.056	0.8710	
D^2	0.00074	1	0.00074	0.036	0.8951	
V^2	0.054	1	0.054	2.64	0.1129	
Residual	0.33	16	0.021	–	–	
Lack of fit	0.27	10	0.027	2.91	0.102	Not significant
Pure error	0.057	6	0.00943			
Total	3.79	30	–	–	–	
R-Squared = 0.9127		Adeq Precision = 13.81				

Table 6
ANOVA analysis of subsurface damages.

Source	SS	DF	MS	F-value	P-value	
Model	94.31	14	6.74	20.14	< 0.0001	Significant
P	29.70	1	29.70	88.82	< 0.0001	
D	4.52	1	4.52	25.48	0.0001	
V	7.37	1	7.37	22.04	0.0002	
F	25.01	1	25.01	74.79	< 0.0001	
*D*V*	3.15	1	3.15	9.42	0.0073	
*V*F*	2.48	1	2.48	7.42	0.0150	
P^2	12.12	1	12.12	36.24	< 0.0001	
F^2	2.81	1	2.81	8.41	0.0105	
V^2	5.19	1	5.19	15.52	0.0012	
*P*D*	0.0056	1	0.0056	0.017	0.8984	
*P*F*	0.11	1	0.11	0.32	0.5819	
*D*F*	0.86	1	0.86	2.56	0.1293	
D^2	0.45	1	0.45	1.36	0.2609	
*P*V*	0.016	1	0.016	0.047	0.8316	
Residual	5.35	16	0.33	–	–	
Lack of fit	3.63	10	0.36	1.27	0.402	Not significant
Pure error	1.72	6	0.29	–	–	
Total	99.66	30	–	–	–	
R-Squared = 0.9463		Adeq Precision = 19.13				

response is plotted by changing only one factor over its range while holding all the other factors constant. From the plot Fig. 15a, it can be found that reduction of surface quality caused by feed rate is more drastic than that by depth of cut. Higher feed rate could reduce the dwell time of laser irradiation on the workpiece, so that it cannot provide enough heat for chemical reaction. Meanwhile, maximum undeformed chip thickness also increases with the increase of depth of cut and workbench feed rate. Hence, the critical cutting depth for occurring ductile to brittle fracture transition of RB-SiC ceramcis could be reached. In contrast, R_a decreases with the increase of laser power and wheel speed in an exponential form. This trend can be explained from two aspects: (a) In the first stage, the reduction strength zone of RB-SiC ceramics was enlarged by laser radiation (b) Subsequently, higher wheel speed could reduce UCT and increase grinding wheel wear which due to longer accumulated sliding length. Previous study showed that when wheel wear down, more grains become active and more cutting edges become dull and flattened [22]. Thereby, ductile flow could dominate the whole removal process in LAG. So the wheel speed is inverse proportion to surface roughness R_a like in CG.

The results of ANOVA of subsurface damage shown in Table 6 indicate that laser power is the most influential factor with the highest F-value of 88.82, following by feed rate, depth of cut and wheel speed. As for second order term, the laser power (P^2), feed rate (F^2) and wheel speed (V^2) are significant in sequence. Fig. 15b shows that when laser power is up to 50 W, the depth of subsurface damage is approximately reduced by 28%. It can be seen that the influence of each individual factor on D_{sub} is very similar to its effect on surface roughness R_a. This observation is consistent with early report that surface roughness R_a is direct correlation with D_{sub} in the grinding of brittle materials.

Usage of 3-D isohipsurface graphs is able to investigate the interaction effects of significant factors on surface roughness R_a and D_{sub}. According to Fig. 16, lower surface roughness R_a can be obtained when higher laser power, higher wheel speed, lower feed rate or depth of cut were employed. The interactive effect of wheel speed and depth of cut has the lowest influence on surface roughness R_a (0.9–1.1 μm) within the range of test parameters. Whereas, the synthetic effect of laser power and feed rate can remarkably decrease R_a value from 1.64 μm to 0.64 μm. These results provide further proof that the surface generated by LAG has excellent advantages compared with CG as shown in Fig. 8. Likewise, the interactive effect of laser power with other factors on D_{sub} is in the similar situation as found for surface roughness. Thus, only the significant interactive term constructed response surface plots are listed as shown in Fig. 17. It indicates that the minimized D_{sub} requires a lower depth of cut cooperating with optimum feed rate and wheel speed.

4.4. Multi-object optimization using genetic algorithms (GA)

In most cases, the objective of rough machining is always achieving high machining efficiency while ensure surface roughness R_a and D_{sub}

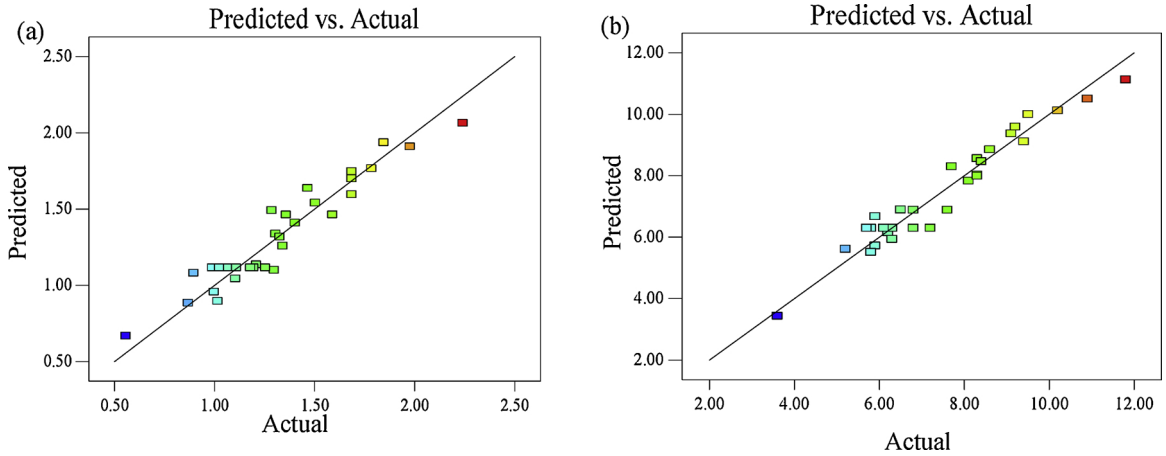

Fig. 13. Predicted vs. actual response plot of (a) R_a and (b) D_{sub}.

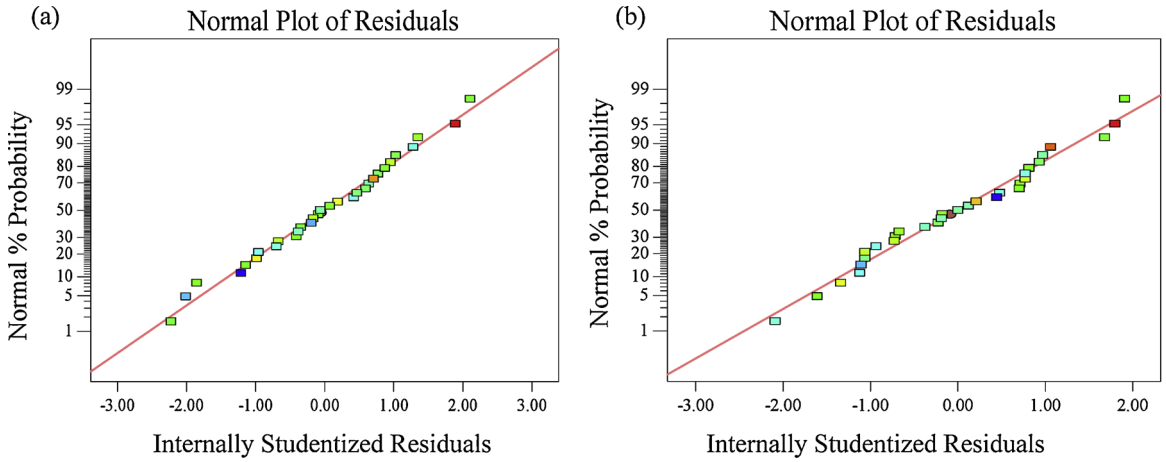

Fig. 14. Probability distribution of standard residual (a) R_a and (b) D_{sub}.

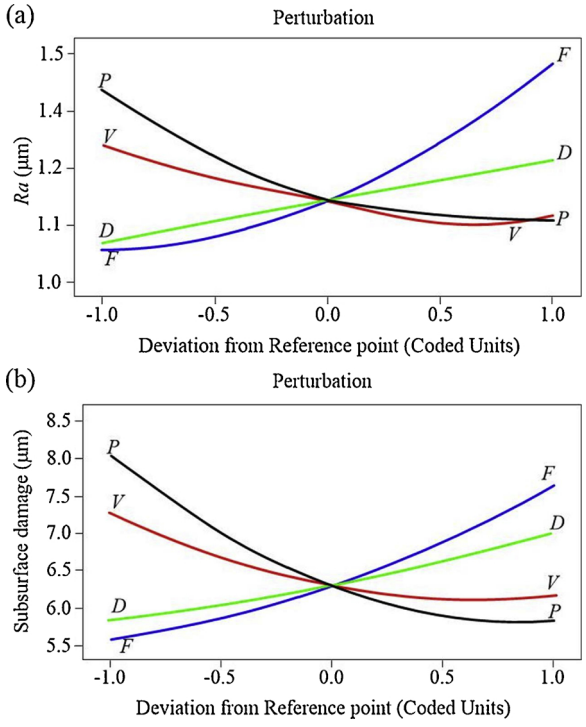

Fig. 15. Effects of influential factors on the R_a and D_{sub} were shown in Perturbation plot.

within the permissible limits. But it is very difficult to achieve this objective in the real due to constraints imposed on machining conditions. In this study, this multi-objective optimization problem is simplified as a single-object problem by applying the weighted sum method. A compromise among each individual objects is made. The individual objective functions are combined into a single composite function. Afterwards, GA was chosen to identify the best solutions in view of different targets because of its greater ability in finding global optimal solutions than other algorithm. Although other differential evolution algorithm is very effective in finding relatively good neighbourhoods of solution in a complex search space, they may have premature convergence towards a local minimum [26].

The desirability function of the smaller the better of normalized error can be formulated as given by Eq. (11):

$$U(P, F, D, W) = W_{Ra}\left(\frac{R_a - R_a'}{R_a'}\right) + W_{D_{sub}}\left(\frac{D_{sub} - D_{sub}'}{D_{sub}'}\right) + W_{M_R}\left(\frac{M_R' - M_R}{M_R'}\right) \quad (11)$$

Where R_a', D_{sub}' and W_{M_R} are the constraints as listed in Table 7. W_{R_a}, $W_{D_{sub}}$ and W_{M_R} are weighting factors deemed as contribution ratio of R_a, D_{sub} and M_R in LAG, respectively. And the weight coefficient determined by different emphasis aspect proposed on account of per requirement of manufacturers.

The details of GA setting parameters are described in Part 2. The final optimum variables results, surface roughness R_a and D_{sub} responses with four interested groups of weight coefficient combinations were tabulated in Table 8. Moreover, in order to visualize the results, a two-dimensional graph was constructed, which chosen laser power and scanning velocity as the x and y coordinate axes, while maintaining other two variables at their optimal levels. Fig. 18 presents the contour plots of the feasible regions and optimum values for the calculation results.

The plots drawn in Fig. 18b and c are the optimization results of Group 2 and 3 when the surface roughness R_a and D_{sub} are given 0.8 weight coefficients. It shows that when material removal rate lies at thresholds, both surface roughness R_a and D_{sub} could reach the minimum. It should be noted that in both cases the optimum variables and response results are approximately the same which fully testifies the positive correlation between surface roughness R_a and D_{sub}. Fig. 18a illustrates that while each individual object occupies the 1/3 proportion, the optimum response located at the middle position in the feasible region. It can also be found in group 4 that the material removal rate can reach about 254.7 mm^3/mm min which is more than two times of the minimum value while satisfying R_a and D_{sub}, achieving 1.179 μm and 6.585 μm, respectively. In this case, the scanning velocity plays a predominant role in achieving high removal rate. The effect of laser power on R_a and D_{sub} is similar to the situation that encountered at group 2 and 3. According to the aforementioned discussions, it can be concluded that surface roughness R_a and D_{sub} could achieve optimum value by adopting appropriate LAG variable parameters with customized weight coefficient.

4.5. Confirmation experiments

The purpose of the confirmation experiments is to validate the accuracy of the predictive model. Four optimum tests were conducted. Each test was performed three times. The comparison of the final average results of measured values of surface roughness R_a and depth of subsurface damage and predicted value by the quadratic models are shown in Fig. 19.

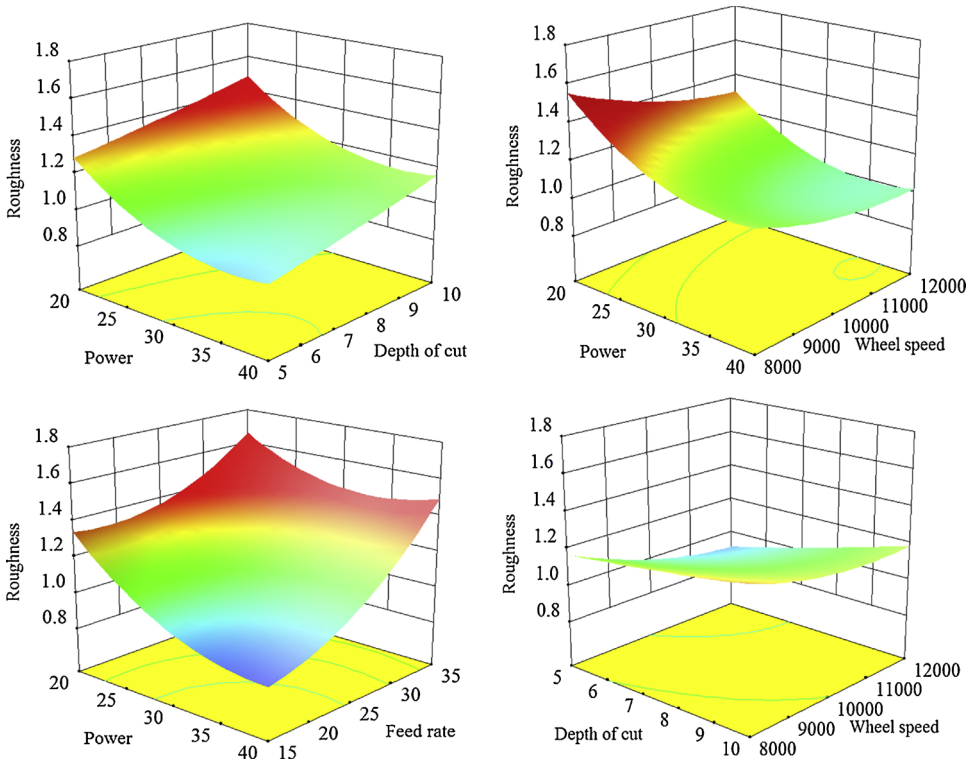

Fig. 16. Surface roughness R_a three-dimensional response surface plots and contour of the test parameters:(a) laser power and depth of cut; (b) laser power and wheel speed; (c) laser power and feed rate; (d) depth of cut and wheel speed.

The percentage error range between the experimental results and the predicted values for R_a is 4.3%–8.7% and D_{sub} is 5.6%–11.6%. Moreover, the experimental average values dispersion is small as described by the standard deviations in Fig. 19, which means the prediction is stability and reasonably accurate. It is reasonable to believe that RSM and GA are effective for developing empirical formula and optimum operating parameter for LAG.

5. Conclusions

1 The transient three-dimensional finite element model for laser preheating in LAG can accurately predict the temperature in the laser radiated zone, with only 2.7%–15.8% prediction error. The microhardness of RB-SiC ceramics decreased from 2917 Hv to 2483 Hv with the increase of laser power from 20 W to 70 W.
2 In comparison with CG, LAG is very effective in reducing grinding force, surface roughness of Ra and subsurface damage. The ductile material removal mode could dominate LAG process of RB-SiC ceramics, if suitable temperature and proper machining conditions are adopted. Two types of grinding-induced subsurface micro-cracks are identified in CG of RB-SiC ceramics, i.e. median and lateral cracks. Nevertheless, only lateral cracks can be observed in LAG of RB-SiC ceramics and penetrate depth is much shallower than the median cracks induced by CG under the same operating conditions.
3 EDS and XRD test demonstrates that oxidation reaction of RB-SiC ceramic occurred prior to grinding process by laser radiation in the

Table 7
Constraints used in the optimization.

Variables	Limits
Laser Power (W)	10–100
Depth of Cut (μm)	5–12.5
Wheel Speed (rpm)	6000–14,000
Feed rate (mm/min)	5–35
Surface roughness (μm)	1.2
Subsurface damage (μm)	7
Material Removal rate (mm^3/mm min)	100

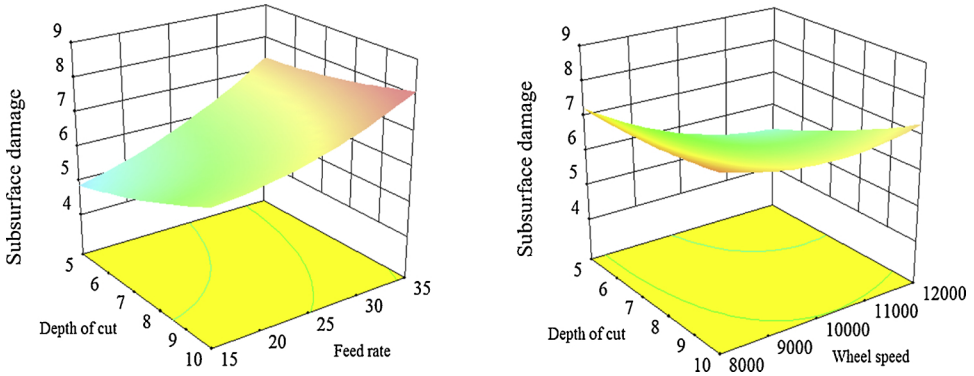

Fig. 17. 3-D plots of the interactive effect on D_{sub} (a) depth of cut and feed rate (b) depth of cut and wheel speed.

Table 8
Optimum machining conditions for multi-performance with different weighting factors.

Process condition number	Weighting factors			Optimization results						
				Cutting conditions				Machining performance		
	W_{Ra}	W_{Sub}	W_M	P(W)	F(mm/min)	V(rpm)	D(μm)	Ra(μm)	D_{Sub}(μm)	M_R(mm^3/mm min)
1	1/3	1/3	1/3	38.98	21.33	8616	7.93	1.047	6.198	169.1
2	4/5	1/5	1/5	38.32	18.87	12,034	5.33	0.742	4.009	100.6
3	1/5	4/5	1/5	38.56	17.21	12,609	5.82	0.745	3.961	100.3
4	1/5	1/5	4/5	37.00	25.58	9994	9.56	1.179	6.585	254.7

oxygen-containing atmosphere, which could lower the material fracture strength.

4 ANOVA analysis reveals that feed rate is the most influential process parameter for surface roughness R_a, followed by laser power, depth of cut and wheel speed. In the case of subsurface damage, the laser power is the most influential factor along with feed rate, depth of cut and wheel speed. Besides, the surface roughness R_a is positive correlation with depth of subsurface damage.

5 The 2-D perturbation plots highlight that within the chosen parameters both surface roughness R_a and subsurface damage depth decreases with the increase of laser power and wheel speed, or decrease of feed rate and depth of cut. The 3-D contour plots indicate that the interactive effect of laser power and feed rate, depth of cut and wheel speed are the most significant on surface roughness Ra and subsurface damage, respectively.

6 The optimization operating parameters calculated using GA with weighted sum method enable the surface roughness R_a and subsurface damage achieve minimum value at the same time ensuring machining efficiency reach maximum.

7 Mathematical models of surface roughness R_a and subsurface damage depth developed using RSM are confirmed with the experiments that conducted at optimum conditions. The results show that the percentage error range between the experimental results and the predicted values at the optimal combination of parameter settings is 4.3%–8.7% and 5.6%–11.6% for R_a and D_{sub}. Therefore, RSM is an effective tool for the analysis of LAG RB-SiC and the developed models are acceptable to predict the LAG output responses.

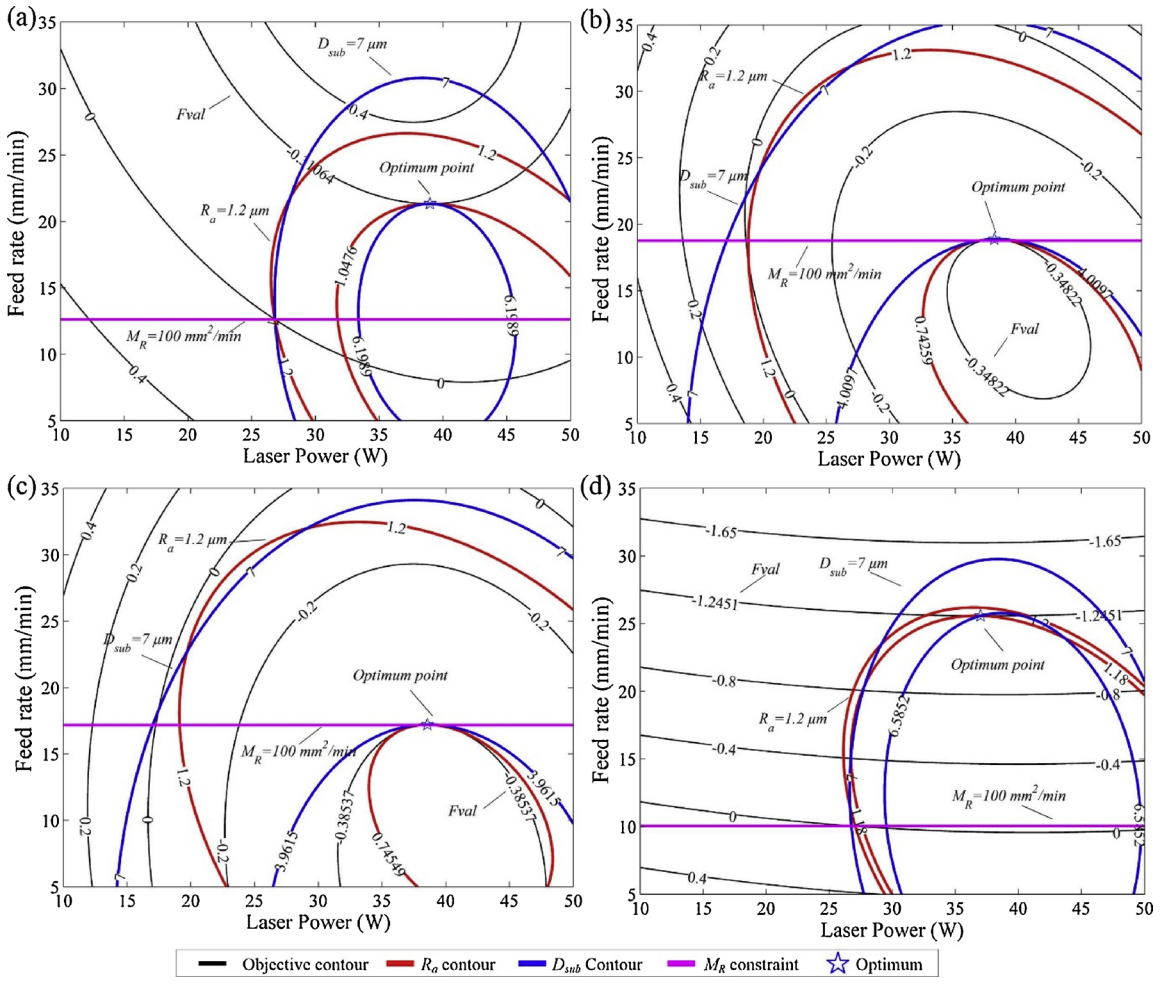

Fig. 18. The plots constructed by optimization, constraints and objective contour. a to d corresponding the process condition 1–4 listed in Table 8.

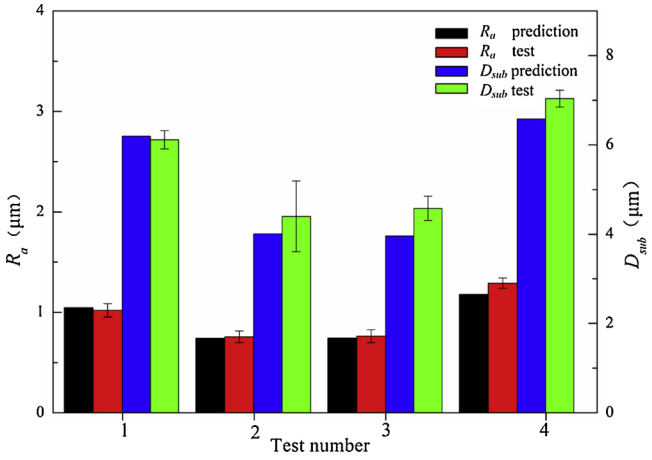

Fig. 19. Comparison of surface roughness and depth of subsurface damage obtained from the confirmation trials and the RSM prediction models.

Acknowledgements

The authors would like to thank the financial from Self-Planned Task (NO. SKLRS201717A) of State Key Laboratory of Robotics and System (HIT), National Key Research and Development Program of China (2016YFB1102204) and the EPSRC project (EP/K018345/1) in the UK for this study.

References

[1] J. Wade, S. Ghosh, P. Claydon, H. Wu, Contact damage of silicon carbide ceramics with different grain structures measured by Hertzian and Vickers indentation, J. Eur. Ceram. Soc. 35 (2015) 1725–1736.
[2] B. Zhang, X.L. Zheng, H. Tokura, M. Yoshikawa, Grinding induced damage in ceramics, J. Mater. Process. Technol. 132 (2003) 353–363.
[3] A.N. Samant, N.B. Dahotre, Laser machining of structural ceramics—a review, J. Eur. Ceram. Soc. 29 (2009) 969–993.
[4] B. Denkena, A. Wippermann, S. Busemann, M. Kuntz, L. Gottwik, Comparison of residual strength behavior after indentation, scratching and grinding of zirconia-based ceramics for medical-technical applications, J. Eur. Ceram. Soc. 38 (2018) 1760–1768.
[5] A. Zahedi, T. Tawakoli, J. Akbari, Energy aspects and workpiece surface characteristics in ultrasonic- assisted cylindrical grinding of alumina – zirconia ceramics, Int. J. Mach. Tools Manuf. 90 (2015) 16–28.
[6] W.L. Chang, X.C. Luo, Q.L. Zhao, J.N. Sun, Y. Zhao, Laser assisted micro grinding of high strength materials, Key Eng. Mater. 496 (2012) 44–49.
[7] C. Chang, C. Kuo, An investigation of laser-assisted machining of Al_2O_3 ceramics planning, Int. J. Mach. Tools Manuf. 47 (2007) 452–461.
[8] G. Guerrini, A.H.A. Lutey, S.N. Melkote, A. Fortunato, High throughput hybrid laser assisted machining of sintered reaction bonded silicon nitride, J. Mater. Process. Technol. 252 (2018) 628–635.
[9] F.E. Pfefferkorn, Y.C. Shin, F.P. Incropera, Laser-assisted machining of magnesia-partially-stabilized zirconia, J. Manuf. Sci. Eng. 126 (2004) 42–51.
[10] Y. Wang, L.J. Yang, N.J. Wang, An investigation of laser-assisted machining of Al_2O_3 particle reinforced aluminum matrix composite, J. Mater. Process. Technol. 129 (2002) 268–272.
[11] S. Lee, J. Kim, J. Suh, Microstructural variations and machining characteristics of silicon nitride ceramics from increasing the temperature in laser assisted machining, Int. J. Precis. Eng. Manuf. Technol. 15 (2014) 1269–1274.
[12] S. Lei, Y.C. Shin, F.P. Incropera, Deformation mechanisms and constitutive modeling for silicon nitride undergoing laser-assisted machining, Int. J. Mach. Tools Manuf. 40 (2000) 2213–2233.
[13] S. Lei, Y.C. Shin, F.P. Incropera, Experimental investigation of thermo-mechanical characteristics in laser assisted machining of silicon nitride ceramics, J. Manuf. Sci. Eng. 123 (2001) 639–646.
[14] C.R. Dandekar, Y.C. Shin, Multi-scale modeling to predict sub-surface damage applied to laser-assisted machining of a particulate reinforced metal matrix composite, J. Mater. Process. Technol. 213 (2013) 153–160.
[15] R. Singh, M.J. Alberts, S.N. Melkote, Characterization and prediction of the heat-affected zone in a laser-assisted mechanical micromachining process, Int. J. Mach. Tools Manuf. 48 (2008) 994–1004.
[16] R.G. Munro, Material properties of a sintered α-SiC, J. Phys. Chem. Ref. Data 26 (1997) 1195–1203.
[17] D. Alfano, L. Scatteia, S. Cantoni, M. Balat-Pichelin, Emissivity and catalycity measurements on SiC-coated carbon fibre reinforced silicon carbide composite, J. Eur. Ceram. Soc. 29 (2009) 2045–2051.
[18] W. Tan, M. Adducci, C. Petorak, B. Thompson, A.E. Brenner, R.W. Trice, Effect of rare-earth dopant (Sm) concentration on total hemispherical emissivity and ablation resistance of ZrB 2/SiC coatings, J. Eur. Ceram. Soc. 36 (2016) 3833–3841.
[19] D. Liu, C. Huang, J. Wang, H. Zhu, P. Yao, Z. Liu, Modeling and optimization of operating parameters for abrasive waterjet turning alumina ceramics using response surface methodology combined with Box – Behnken design, Ceram. Int. 40 (2014) 7899–7908.
[20] S. Agarwal, Optimizing machining parameters to combine high productivity with high surface integrity in grinding silicon carbide ceramics, Ceram. Int. 42 (2016) 6244–6262.
[21] I. Shigematsu, K. Kanayama, A. Tsuge, M. Nakamura, Analysis of constituents generated with laser machining of Si_3N_4 and SiC, J. Mater. Sci. Lett. 17 (1998) 737–739.
[22] L. Yin, H. Huang, K. Ramesh, T. Huang, High speed versus conventional grinding in high removal rate machining of alumina and alumina – titania, Int. J. Mach. Tools Manuf. 45 (2005) 897–907.
[23] N. Senthilkumar, T. Tamizharasan, V. Anandakrishnan, Experimental investigation and performance analysis of cemented carbide inserts of different geometries using Taguchi based grey relational analysis, Measurement 58 (2014) 520–536.
[24] P. Sahoo, Modeling and optimization of surface roughness and tool vibration in CNC turning of Aluminum alloy using hybrid RSM-WPCA methodology, Int. J. Ind. Eng. Comput. 8 (2017) 385–398.
[25] W. Ding, J. Xu, Z. Chen, Wear behavior and mechanism of single-layer brazed CBN abrasive wheels during creep-feed grinding cast nickel-based superalloy, Int. J. Adv. Manuf. Technol. 51 (2010) 541–550.
[26] A.R. Yildiz, A new hybrid differential evolution algorithm for the selection of optimal machining parameters in milling operations, Appl. Soft Comput. J. 13 (2013) 1561–1566.